Joukowski's wake model for tip-splitting rotors

To cite this article: A Castillo-Castellanos *et al* 2021 *J. Phys.: Conf. Ser.* **1934** 012005

View the article online for updates and enhancements.

Joukowski's wake model for tip-splitting rotors

A Castillo-Castellanos[1], E Durán Venegas[2], and S Le Dizès[1]

[1] Aix Marseille Université, CNRS, Centrale Marseille, IRPHE, 49, rue Frédéric Joliot-Curie, BP146, 13384 Marseille, France
[2] Departamento de Bioingeniería e Ingeniería Aeroespacial, Universidad Carlos III de Madrid, Escuela Politécnica Superior, Avda. de la Universidad, 30. 28911 Leganés, Spain

E-mail: andres-alonso.castillo-castellanos@univ-amu.fr

Abstract. The interaction between a tip vortex and a solid surface is responsible for premature structural component fatigue in wind turbines and undesirable noise in helicopter rotors during low speed and descending flight. One noise reduction strategy uses a modified airfoil to split and spread the vorticity in two tip vortices. The present paper aims to provide the wake structure produced by such a rotor for wind turbine and helicopter regimes. We use a filamentary approach, such that vortices are assumed to roll-up quickly to form thin vortex filaments of finite but small size and compute the induced velocity using a cut-off method. The structure of the wake is analyzed in the near- and far-fields separately. It is found to have a dual nature and to be well-described by a twisted vortex pair locally aligned along with a larger helical structure. The linear stability of the far-wake with respect to long-wave displacements is also analyzed. Two kinds of instability modes are obtained associated with a pairing between successive turns of the large helical structure and a pairing between successive turns of the vortex pair.

1. Introduction

Rotating blades, such as those of a helicopter rotor or a horizontal-axis wind turbine, generate concentrated vortices at their tips, transported downstream, creating a helical pattern. These helical vortices are associated with several practical issues actively investigated. One of these issues concerns the interaction between a tip vortex and a rotor blade (Blade-Vortex Interaction, BVI), which causes significant noise and vibration problems. One approach to mitigate BVI noise is to introduce a modified vane tip to split the tip vortex into two, (see, for instance [1]). The degree of interaction between the two vortices depends on the relative strength and the separation distance. For weakly interacting pairs, the rotor wake deviates little from the helical shape. However, for strongly interacting pairs, the rotor wake resembles a braided pattern where a small helical pair is inscribed on top of a larger helix [2]. Similarly to the case of vortex rings and helical vortices, this structure can rotate and translate by self-induction without deformation. The stability of such structure has practical relevance, since instabilities may contribute to accelerate the merging process, vortex diffusion and the transition towards a turbulent wake.

From a theoretical perspective, the stability properties of uniform helices have been the subject of numerous works. Instabilities found in uniform helical vortices can be broadly classified as short-wave and long-wave instabilities [3]. Short-wave instabilities, such as the elliptic instability [4, 5] or the curvature instability [6, 7], originate by a deformation of the vortex core. On the other hand, long-wavelength instabilities are characterized by a local displacement of the vortex, without changing the internal core structure. For uniform helices, the most

unstable perturbations are those for which displacements of consecutive turns are out of phase [8, 9]. More recently, Duràn Venegas & Le Dizès [10] used numerical simulations to obtain general solutions for helical pairs of different pitch and radius ratios. This approach was used to characterize the stability properties of the wake for the wind turbine and helicopter flight regimes [11] consistent with experimental results in a water channel [17, 10]. Perturbations were found to be quickly advected away from the rotor, such that stability properties are consistent with theoretical predictions for the far-wake (uniform helices in the case of [11]).

For this work, we study the long-wavelength stability for the wake produced by a tip-splitting rotor blade. In particular, we use a filamentary approach to address the linear stability of pairs of closely spaced helical vortices obtained in [2]. Base solutions are characterized by a rotation of the vortex pair as it moves along a large-scale helical motif. From afar, the vortex structure is reminiscent of a helical vortex but in a closer view, it resembles a helical vortex pair aligned with the locally tangent flow. Given these similarities, we expect the solutions to display features from both systems. In particular, to be linearly unstable and display two kinds of local pairing instability: of the successive turns of the large-scale pattern, and the successive turns of the vortex pair.

2. Framework

2.1. Vortex filament framework

The present work is based on a vortex filament approach [10, 11, 2]. All the vorticity is concentrated in thin vortex filaments which move as material lines in the fluid according to

$$\frac{d\vec{X}_j}{dt} = \vec{U}^{ind}(\vec{X}_j) + \vec{U}^\infty \tag{1}$$

where $\vec{X}_j = (r_j, \theta_j, z_j)$ is the position vector of the j-th vortex filament, $\vec{U}^{ind}$ is the induced velocity and $\vec{U}^\infty$ an external velocity field. Each vortex is discretized in segments $[\vec{X}_j^n, \vec{X}_j^{n+1}]$. The induced velocity is obtained using Biot-Savart with a cutoff approach and a Gaussian vorticity profile. The precise expressions that we use are given in [10].

We are interested in stationary solutions in the rotor frame, in the sense that the vortex structure and the velocity field are steady, but the vortex elements are moving along the steady vortex structure. This condition of steadiness is written as

$$\frac{dr_j}{d\zeta} = \frac{U_r^{ind}(\vec{X}_j)}{\Omega_R}, \quad \frac{d\theta_j}{d\zeta} = \frac{\Omega^{ind}(\vec{X}_j) - \Omega_R}{\Omega_R}, \quad \frac{dz_j}{d\zeta} = \frac{U_z^{ind}(\vec{X}_j) - U_z^\infty}{\Omega_R} \tag{2}$$

where Ω_R is the rotation rate of the rotor and vortices are parametrized in terms of the wake age $\zeta = \Omega_R(t - t_0)$ as proposed by [13]. These systems are to be solved with boundary conditions on the rotor (at $\zeta = 0$) where the position of each vortex is prescribed, and far-field boundary conditions at $\zeta \to \infty$. These last boundary conditions are not trivial as the far-field is a priori unknown. Therefore, our first task is to characterize the far-field.

2.2. Solutions in the far-field

We consider solutions that are created by the emission of two closely-spaced co-rotating vortices from a rotating blade tip under an external axial flow. One expects close to the rotor for a global contraction (resp. expansion) of the structure during a climbing helicopter (resp. wind turbine) regime, whereas in the far-field, a quasi-uniform regime is expected.

Let us consider two vortices of circulations Γ_1 and Γ_2 prescribed at the radial coordinates R_1 and $R_2 = R_1 - d$, respectively. For cases for which $\Gamma_1 + \Gamma_2 \neq 0$, the vortices are expected to rotate around the invariant vorticity center

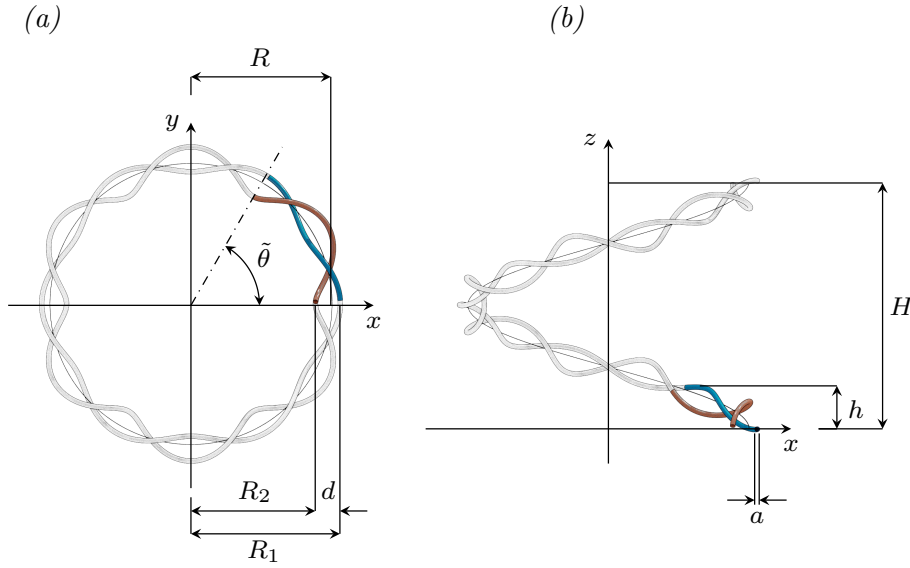$$R = \frac{\Gamma_1 R_1 + \Gamma_2 R_2}{\Gamma_1 + \Gamma_2} \tag{3}$$

Figure 1. Three-dimensional representation of the vortex structure corresponding to far-field solutions defined only by geometric parameters: separation distance d, radii R_1, R_2, and R, vortex core size a, axial pitches H and h, and twist parameter $\beta = \pm 2\pi/\tilde{\theta} = H/h$. (a,b) View in the (x, y) and (x, z) planes, respectively.

as they are advected by the mean flow. This motion creates a pair of interlaced helices of radii

$$\rho_1 = (R_1 - R), \quad \rho_2 = d - \rho_1 \tag{4}$$

and pitch h_τ (corresponding to an axial pitch h), inscribed on a larger underlying helix of radius R and pitch H. This applies to co-rotating pairs, where $R_1 < R < R_2$, and for counter-rotating pairs, where $R < R_1$. For this work, we focus on the co-rotating case. Another important parameter is the ratio $\beta = H/h$ measuring the number of turns of the vortex pair per one turn of the larger helical pattern. Such idealized structure is defined by the geometric parameters identified in figure 1. The space-curves $\vec{X}_j$ described by the double-helix as a function of the angular coordinate θ_0 are given by

$$x_j = (R + \rho_j \cos \phi_j) \cos \theta_0 - c_\tau \rho_j \sin \phi_j \sin \theta_0 \tag{5}$$
$$y_j = (R + \rho_j \cos \phi_j) \sin \theta_0 + c_\tau \rho_j \sin \phi_j \cos \theta_0 \tag{6}$$
$$z_j = (H/2\pi)\theta_0 - c_\kappa \rho_j \sin \phi_j \tag{7}$$

where $\phi_1 \equiv \beta\theta_0$ and $\phi_2 \equiv \beta\theta_0 + \pi$ defines the orientation relative to the x-axis (representing the chord plane), while

$$c_\tau \equiv \frac{|H|}{\sqrt{H^2 + 4\pi^2 R^2}}, \quad c_\kappa \equiv \frac{2\pi R}{\sqrt{H^2 + 4\pi^2 R^2}} \tag{8}$$

are related to the torsion curvature coefficients, respectively.

The above structure satisfies the following form of spatial periodicity: it is invariant by the double operation $z_j \to z_j + h$ and $\theta_j \to \theta_j + \tilde{\theta}$, where $\tilde{\theta} = 2\pi/\beta$ is the azimuthal period of the vortex pair. In the following, we keep this property to obtain the proper solutions. Since we do not want the solution to repeat several times in a spatial period, we further assume that, there is a single location over an axial distance h where both vortices are at the same azimuth $\theta_0 = \theta_1 = \theta_2$. We chose this azimuth to define the radius R and separation distance d. The
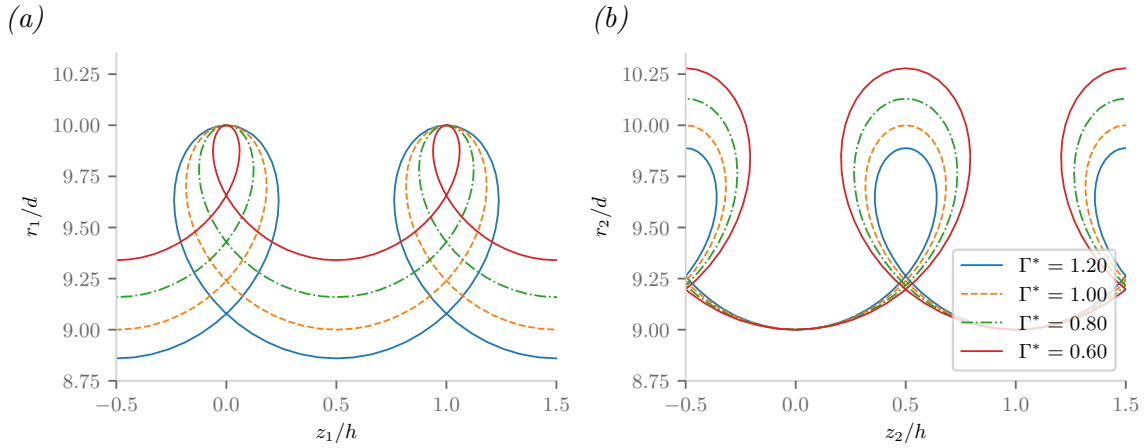
Figure 2. Radial coordinates *(a)* r_1 and *(b)* r_2 as function of the axial coordinate z_j for $H^* = 10$, $h_\tau^* = 8$, $\varepsilon = 0.1$ and $R^* = 9 + 1/(1 + \Gamma^*)$ for different Γ^*.

axial period h then defines a mean axial pitch while H is obtained from $H = 2\pi h/\tilde{\theta}$. In addition to the core size a and circulation Γ_j, these parameters can be used to define five dimensionless parameters

$$R^* \equiv \frac{R}{d}, \quad H^* \equiv \frac{H}{d}, \quad h_\tau^* \equiv \frac{h_\tau}{d}, \quad \varepsilon \equiv \frac{a}{d}, \quad \Gamma^* \equiv \frac{\Gamma_2}{\Gamma_1} \tag{9}$$

that characterize solutions in the far-field. Note that $\Gamma^* = 1$ corresponds to a special case since both vortices may be deemed as interchangeable, such that our periodic domain is further reduced to $\tilde{\theta}/2$ as presented in [2].

With each geometry there is associated a unique moving frame where the solution is steady. The main idea is to find the rotation rate Ω^F and axial speed U_z^F as to counter the rotation of the vortex pair. In practice, this is done by integrating (2) over the interval $\theta_0 \in [0, \tilde{\theta}]$ and applying the corresponding boundary conditions, see [2] for a precise description of the procedure. Since equations (5)-(7) do not fully satisfy the steadiness condition, the helices must deform to be compatible with the self-induced motion. Because of the spatial periodicity, the calculation domain is comprised between $\theta_0 = 0$ and $\theta_0 = \tilde{\theta}$. Our description is completed by the corresponding boundary conditions, $\vec{X}_j = (R_j, 0, 0)$ at $\theta_0 = 0$ and $\vec{X}_j = (R_j, \tilde{\theta}, h)$ at $\theta_0 = \tilde{\theta}$. Equation (2) is solved numerically as a non-linear minimization problem through an iterative procedure using (5)-(7) as initial guess values. In practice, for most calculations we use $p_n = 48$ segments per period.

A typical result of the far-wake is presented in figures 2 and 3 for different circulation ratios. Steady solutions are found for a wide range of parameters and circulation ratios $\Gamma^* \in [0.6, 1.2]$. Here, the value of R^* was chosen to ensure the vortices are emitted at the same radial coordinates, $R_1/d = 10$ and $R_2/d = 9$, respectively. Solutions with $\Gamma^* \neq 1$ are characterized by $\min(r_j) < R_2$ for $\Gamma^* > 1$ and $\max(r_j) > R_1$ for $\Gamma^* < 1$. Solutions are also characterized by a local maxima in the curvature coefficient in vortex 1 for $\Gamma^* < 1$ and vortex 2 for $\Gamma^* > 1$. Deviations from (5)-(7) are more easily appreciated in the local coordinates ρ_j which are no longer constant and equal to (4). As noted in [2], deviations from the prescribed form increase as the role of self-induction becomes prominent (small pitch, large curvature).

2.3. Solutions in the near-field
In this section, we consider the vortex structure close to the rotor plane using the approach described in [11, 2]. Instead of fixing the geometric parameters to find the associated frame
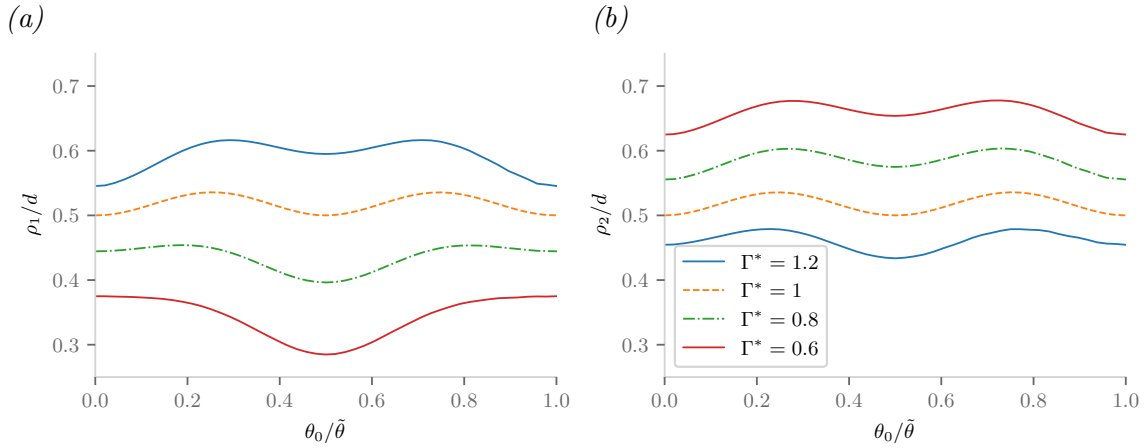
Figure 3. Local coordinates *(a)* ρ_1 and *(b)* ρ_2 as function of θ_0 for the cases in figure 2.

velocities, we solve the inverse problem. That is, we fix the operating conditions (rotation rate Ω^R and external velocity U_z^∞) and compute the corresponding wake geometry. For this section, we use subscripts $(\cdot)_{tip}$ (resp. $(\cdot)_{fin}$) to denote the properties of vortex 1 (resp. 2), whereas subscript $(\cdot)_0$ denotes values corresponding to the rotor plane $\zeta = 0$. The prescribed geometrical parameters are the radial coordinates where the vortices are emitted on the rotor blade, R_{tip} and $R_{fin} = R_{tip} - d_0$. If we add the circulations Γ_{tip} and Γ_{fin}, and the core size a, the resulting problem is governed by five non-dimensional parameters

$$\lambda = \frac{R_{tip}\Omega_R}{U_z^\infty}, \quad \eta = \frac{\Gamma_{tip}}{R_{tip}^2\Omega_R}, \quad R_0^* = \frac{R_0}{d_0}, \quad \varepsilon^* = \frac{a}{d_0}, \quad \Gamma^* = \frac{\Gamma_{fin}}{\Gamma_{tip}} \tag{10}$$

where λ is known as the tip-speed-ratio, η represents the relative vortex strength, and

$$R_0 \equiv R_{tip} - d_0 \frac{\Gamma^*}{1 + \Gamma^*} = R_{fin} + d_0 \frac{1}{1 + \Gamma^*} \tag{11}$$

is the radial location of the vorticity center on the rotor blade. As in [10, 11, 2], we choose a convention such that η remains positive, while λ may change sign. Wind turbine regimes correspond to $\lambda > 0$, while helicopters may correspond to either $\lambda < 0$ in climbing flight or $\lambda > 0$ in descending flight. We consider $R_0^* \gg 1$ and $\varepsilon^* = 0.1$, as to enhance the rotation of the vortex pair, but well below the merging threshold of the vortex pair [14, 15].

The near-field solution satisfies (2) with the boundary condition at $\zeta = 0$, which should match a far-field solution as we go away from the rotor. This condition is implemented as in [10, 2]. The induced velocity is decomposed into contributions from the near-field and far-field. Contributions from the far-field are modeled by imposing that after a certain distance from the rotor plane, the wake adopts the geometry of a far-field solution. The corresponding geometrical parameters are estimated from the near-field solution at the end of calculation domain. The computational domain must be sufficiently large for the wake to develop and match the far-field.

3. Comparison with experimental results
For this section, we perform a qualitative and quantitative comparison between numerical results obtained using the procedure described above, and experimental results from one-bladed rotor equipped with a perpendicular tip fin placed on its pressure side by [16]. Reference values correspond to a wake age $\zeta = 90^o$, close to the rotor plane. The measurements retained for this

Parameters						Measurements at $\zeta = 90^o$		
R_{tip}	24	cm	Γ_{tip}	161	cm^2/s	R	22.5	cm
R_{fin}	21	cm	Γ_{fin}	153	cm^2/s	H	16.8	cm
d_0	3	cm	U_z^∞	11.5	cm/s	d	3.2	cm
a	0.3	cm	Ω^R	2π	Rad/s	$|\beta|$	0.77	

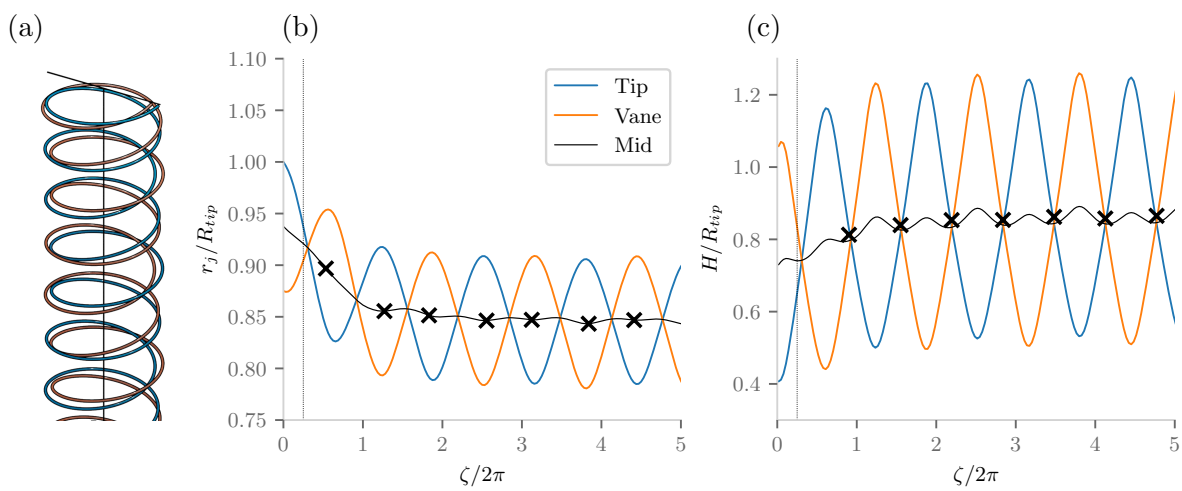**Table 1.** Experimental parameters and measurements from [16].

Figure 4. Steady solution for the parameters in table 1. (a) Schematic representation; Evolution of (b) the radial coordinates r_j and (c) the local pitch H as function of the wake age ζ. Solid marks indicate the points where the vortices are located at the same azimuthal coordinate.
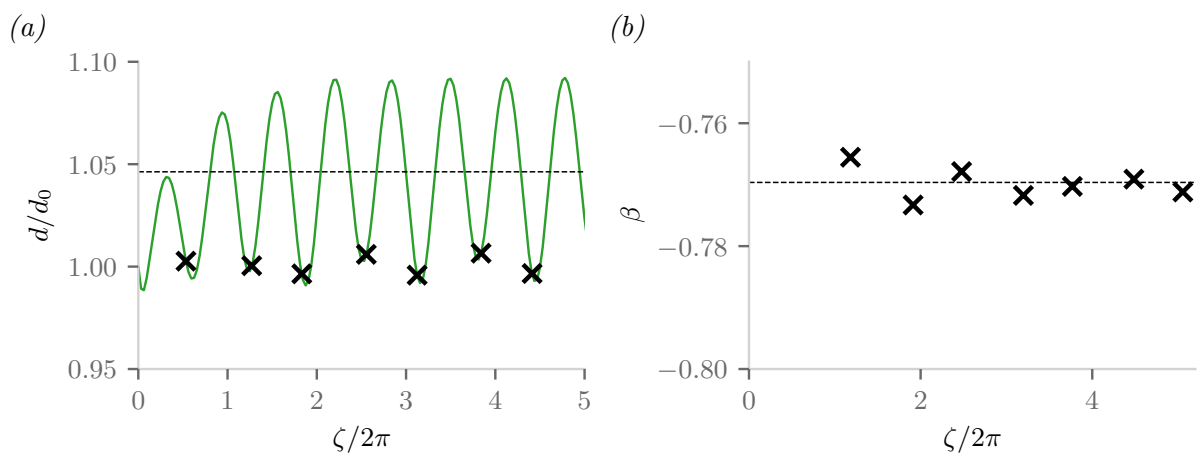

Figure 5. Steady solution for the parameters in table 1. Evolution of *(a)* the separation distance d and *(b)* twist parameter β as function of the wake age ζ.

comparison (table 1) correspond to a climbing helicopter flight regime ($\Gamma^* = 0.95$, $\lambda = -13$, and $\eta = 0.044$) shown in figure 4. The wake is characterized by a radial contraction, while the two vortices trade places continuously with local variations of the axial pitch H also present. A good agreement is observed with experimental measurements close to the rotor plane ($R \approx 22.2$ cm and $H \approx 16.8$ cm compared to the experimental values $R = 22.5$ cm and $H = 16.8$ cm, respectively). As shown in [2], the evolution of both quantities is comparable to that of a equivalent helix with radius R_0 and total circulation $\Gamma_{tot} = \Gamma_{tip} + \Gamma_{fin}$.

Simultaneously, the separation distance is shown to expand roughly by 5% due to the combined effects of the vortex pair and the rotor's presence, while the twist parameter β remains essentially constant (figure 5). Both quantities are also in good agreement with experimental measurements ($\overline{d} \approx 3.14$ cm and $|\beta| \approx 0.77$ compared to $d = 3.2$ cm and $\beta = 0.77$, respectively). As shown in [2], both quantities are mainly driven by the evolution of the large scale. If R and H at the far-field are known, both values can be approximated by

$$\frac{d}{d_0} \approx \left[\frac{1 + \lambda^2}{1 + \lambda^2 R^2 / R_0^2} \right]^{1/4} = 1.08 \qquad |\beta| \approx \frac{\eta R_0^2}{\pi d_0^2} = 0.78 \qquad (12)$$

in good agreement with the numerical and experimental results (table 1).

4. Long-wave instability of the double-helix

In this section, we analyze the evolution of linear perturbations to the base flow obtained above. Since perturbations are expected to be quickly advected away from the rotor, we are interested in the structure observed in the far-field. The stability of such structures with respect to long wavelength perturbations are presented in detail in [19] for the case with $\Gamma^* = 1$.

4.1. Perturbation model

Stability is analyzed by considering the evolution of infinitesimal perturbation displacements

$$\vec{X}_j(\zeta, \psi) = \vec{X}_j^B(\zeta) + \delta \vec{X}_j(\zeta, \psi) \qquad (13)$$

where $\vec{X}_j^B(\zeta)$ corresponds to the base flow obtained in the previous sections, $\delta \vec{X}_j(\zeta, \psi)$ to the perturbation displacements, and $\psi = \Omega_R t$ is a proxy of time [13].

Equation (2) is linearized around $\vec{X}_j^B(\zeta)$ to obtain an approximate locally linear dynamical system

$$\frac{d\vec{q}}{d\psi} = \mathsf{L}\vec{q} \qquad (14)$$

where $\vec{q} = (\delta \vec{X}_1, \delta \vec{X}_2)$ is the total displacement vector and L is the Jacobian of the system obtained using a semi-analytical expression as detailed in [11]. As the base flow is stationary, the operator L is independent of ψ. The long time behavior can therefore be analyzed by looking at normal modes of the form $\psi = \Phi(\zeta) \exp\left((\sigma + i\omega)\psi\right)$ where σ is the growth rate, and ω the frequency.

We are especially interested in the modes that provide the largest growth rate. The spatial structure of these modes is analyzed by performing a Fourier decomposition along ζ.

4.2. Most unstable modes

A typical stability diagram for a case matching the far-wake in table 1 is displayed in figure 6. For this geometry, instability properties are best understood in the frequency spectra. Here, the spectra is characterized by three contiguous lobes at low frequencies, and one additional lobe at higher frequencies. The maximum growth rate is comparable to that of an equivalent
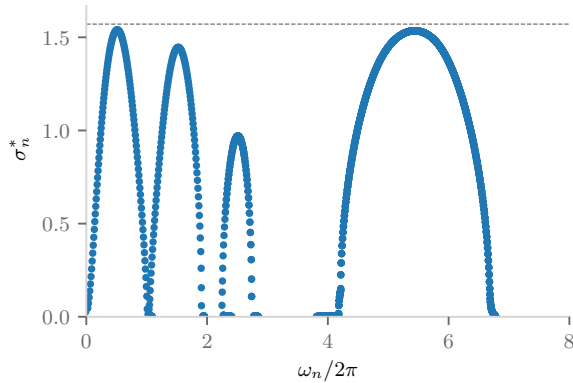
Figure 6. Dimensionless growth rate $\sigma_n^* = \sigma_n(2H^2/\Gamma_{tot}\Omega_R)$ as function of frequency ω_n shown for $R^* = 7$, $H^* = 0.75$, $\beta = 0.75$, $\varepsilon^* = 0.1$, and $\Gamma^* = 0.95$.

helical vortex with $\sigma^* = \sigma(2H^2/\Gamma_{tot}\Omega_R) \sim \pi/2$. The three contiguous lobes cover a fixed range of frequencies, with the maximum growth rates observed close to $\omega = \pm 0.5$, $\omega = \pm 1.5$, and $\omega = \pm 2.5$, respectively. In contrast, the last lobe corresponds to a variable range of frequencies between $\omega = 4.1$ and $\omega = 6.7$, with the most unstable mode at $\omega = \pm 5.4$.

The spatial structure of the unstable deformation modes corresponding to the local maxima are displayed in figure 7. In order to highlight the deformations affecting the large-scale pattern, a tubular section enclosing the two vortices around the vorticity center is also shown. For $\omega = \pm 0.5$ and $\omega = \pm 1.5$, deformations are best described as a periodic local pairing between consecutive turns of the large-scale pattern, see figures 7a-b. Indeed, perturbations are predominantly aligned, i.e., vortices move concomitantly, such that the ensemble is expected to behave like an equivalent helical vortex. If we consider a longitudinal cut, the displacement of the vortices are in phase opposition with respect to their neighbors and make a 45° angle with respect to line connecting both vortices. This behavior is quite general, regardless of individual displacements of $\vec{X}_1$ and $\vec{X}_2$, and of the geometric parameters [19]. In contrast, deformations corresponding to $\omega = \pm 5.4$ are best described as an antisymmetric mode, in the sense that vortices seem to move towards or away from one another in a coordinated manner, while the large-scale pattern remains essentially unchanged, see figure 7c. These modes can be seen as a form of local pairing between the successive turns of the vortex pair [19].

The dominant wavenumbers associated with the most unstable modes are displayed on the right side in figure 7. On the one hand, for modes in the three contiguous lobes, like $\omega = \pm 0.5$ and $\omega = \pm 1.5$, in-phase displacements are clearly predominant, corresponding to azimuthal wavenumbers $k = \mp\omega$. On the other hand, for modes in the last lobe, like $\omega = \pm 5.4$, in-phase and out-of-phase displacements are comparable, with out-of-phase (resp. in-phase) displacements corresponding to $k = \mp\omega$ (resp. $k = \mp(\omega + \beta)$) and additional harmonics. From this point of view, perturbation displacements are shown to propagate as a wave-packet with constant phase velocity $v_p \approx -1$ and zero group velocity [19].

5. Conclusions

In this article, we have obtained using a cut-off filament approach numerical solutions describing the wake generated by a single-bladed tip-splitting rotor for different circulation ratios. These solutions are stationary in the frame rotating with the rotor blade. The structure can be understood as a rotation of the vortex pair around the vorticity center, that is inscribed on a larger helical pattern. Because our solutions are based on a filament description, they do not provide information on the formation of the vortices in the neighborhood of the blade. We have assumed that well-defined and separated vortices are immediately formed behind the blade, and viscous effects are neglected. Despite these simplifications, the wake geometry close to the rotor plane is in good agreement with experimental measurements for a single-bladed rotor by [16].
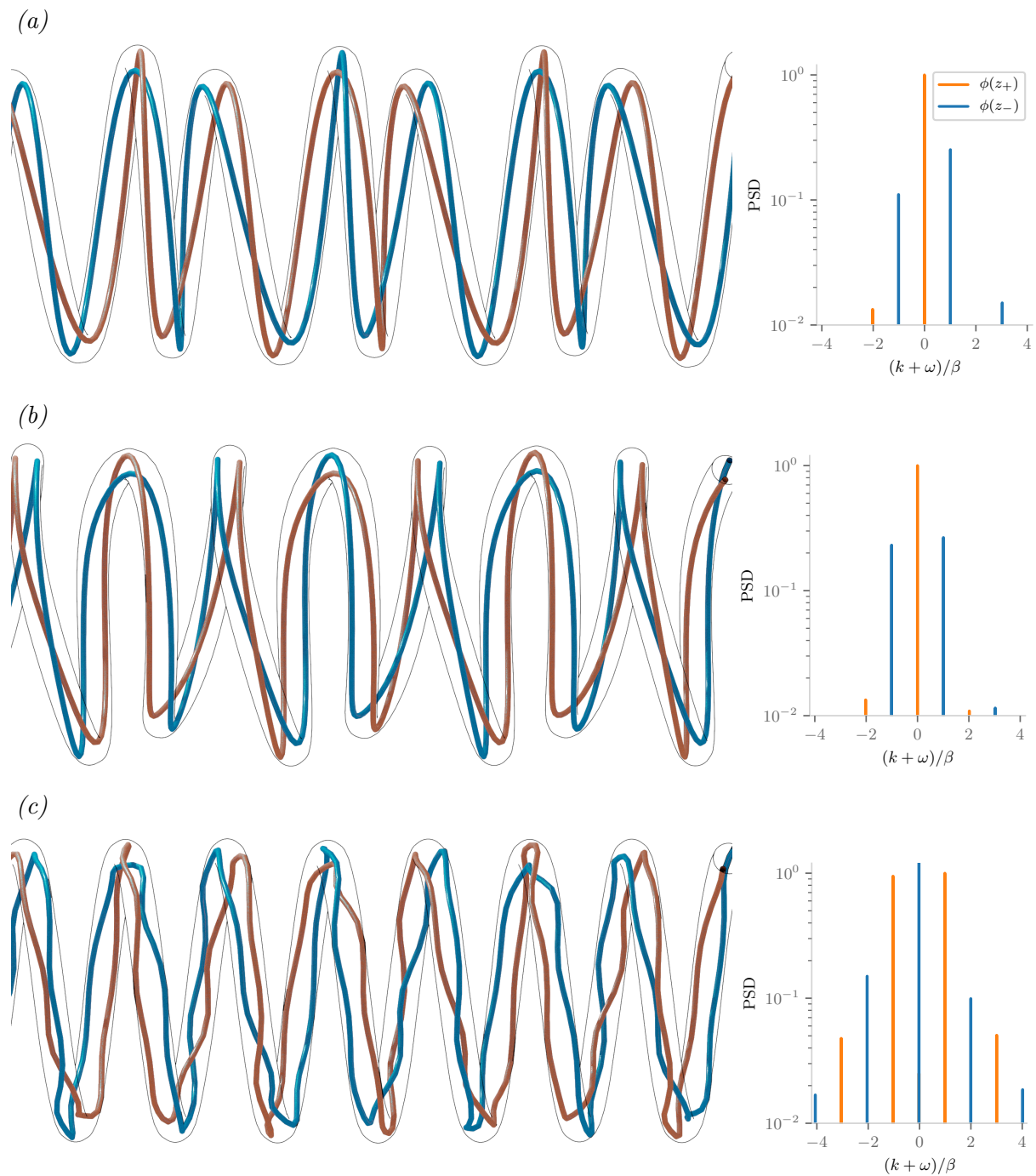
Figure 7. (Left) Most unstable modes the case in figure 6. Fig. *(a)* corresponds to $\omega_n = \pm 0.5$; *(b)* $\omega_n = \pm 1.5$; and *(c)* $\omega_n = \pm 5.4$. A tubular section enclosing the two vortices and centered around the vorticity center is also displayed to highlight the global displacement. (Right) Fourier amplitudes of displacement modes in the axial direction, color indicates in-phase (resp. out-of-phase) displacements in blue (resp. orange).

We also considered the stability of the solutions to perturbations whose wavelength is large relative to the vortex core size. In most cases, the most unstable modes are related to the local pairing of consecutive turns and that growth rates can be predicted from an 'equivalent' helical vortex. A second type of unstable modes, which modify the separation distance between the vortex pair is also observed. For these modes, the growth rates are comparable to the local pairing modes, but excite shorter wavelengths selected by the wake geometry.

Acknowledgments

References

[1] Brocklehurst A and Barakos GN 1994 *Prog. Aerosp. Sci.* **56** 35-74
[2] Castillo-Castellanos A, Durán Venegas E and Le Dizès S 2021 Submitted to *Phys. Rev. Fluids*
[3] Leweke T, Quaranta HU, Bolnot H, Blanco-Rodríguez FJ and Le Dizès S 2014 *J. Phys.: Conf. Series* **524** 012154
[4] Kerswell R 2002 *Annu. Rev. Fluid Mech.* **34** 83-113
[5] Blanco-Rodríguez FJ and Le Dizès S 2016 *J. Fluid Mech.* **804** 224-247
[6] Hattori Y and Fukumoto Y 2009 *Phys. Fluids* **21** 014104
[7] Blanco-Rodríguez FJ and Le Dizès S 2017 *J. Fluid Mech.* **814** 397-415
[8] Widnall SE 1972 *J. Fluid Mech.* **54** 641-663
[9] Gupta BP and Loewy RG 1974 *AIAA J.* **12** 1381–1387
[10] Durán Venegas E and Le Dizès S 2019 *J. Fluid Mech.* **865** 523-545
[11] Durán Venegas E, Rieu P and Le Dizès S 2021 *J. Fluid Mech.* **911** A6
[12] Quaranta HU, Bolnot H and Leweke T 2015 *J. Fluid Mech.* **780** 687-716
[13] Leishman JG 2016 *Principles of Helicopter Aerodynamics* (Cambridge University Press)
[14] Meunier P, Ehrenstein U, Leweke T and Rossi M 2002 *Phys. Fluids* **14** 2757-2766
[15] Meunier P, Le Dizès S, and Leweke T 2005 *C R Phys* **6** 431-450
[16] Schröder D, Leweke T, Hörnschemeyer R and Stumpf E 2021 *AIAA Scitech 2021 Forum* 1088
[17] Quaranta HU, Bolnot H and Leweke T 2015 *J. Fluid Mech.* **780** 687–716
[18] Quaranta HU, Brynjell-Rahkola M, Leweke T, and Henningson DS 2019 *J. Fluid Mech.* **863** 927–955
[19] Castillo-Castellanos A, Durán Venegas E and Le Dizès S 2001 Submitted to *Phys. Rev. Fluids*